CONDENSED MATTER PHYSICS

Persistent coherence of quantum superpositions in an optimally doped cuprate revealed by 2D spectroscopy

Fabio Novelli[1,2], Jonathan O. Tollerud[1], Dharmalingam Prabhakaran[3], Jeffrey A. Davis[1,4]*

Quantum materials displaying intriguing magnetic and electronic properties could be key to the development of future technologies. However, it is poorly understood how the macroscopic behavior emerges in complex materials with strong electronic correlations. While measurements of the dynamics of excited electronic populations have been able to give some insight, they have largely neglected the intricate dynamics of quantum coherence. Here, we apply multidimensional coherent spectroscopy to a prototypical cuprate and report unprecedented coherent dynamics persisting for ~500 fs, originating directly from the quantum superposition of optically excited states separated by 20 to 60 meV. These results reveal that the states in this energy range are correlated with the optically excited states at ~1.5 eV and point to nontrivial interactions between quantum many-body states on the different energy scales. In revealing these dynamics and correlations, we demonstrate that multidimensional coherent spectroscopy can interrogate complex quantum materials in unprecedented ways.

INTRODUCTION

Understanding and controlling the properties of quantum materials is an outstanding challenge for contemporary science and could result in enormous technological returns (*1*). Quantum many-body materials characterized by strong electronic correlations display a multitude of intriguing phases with unique electric and magnetic features, including the Mott transition, colossal magnetoresistance, topological insulators, and high-temperature superconductivity. These macroscopic properties emerge out of microscopic complexity (*2*), which is rooted in the competing interactions between the degrees of freedom (DOF) (charge, lattice, spin, orbital, and topology) of a large number of electronic states. The balance between these DOF can be tipped by, for example, photodoping, causing marked changes to the macroscopic properties, for example, turning an insulator into a metal (*3*).

To address the interactions between the different DOF in the prototypical strongly correlated cuprates, a variety of pump-probe time-resolved experiments have been used (*4*–*7*). These measurements have been used to map the dynamics of excited electronic populations and quantify the charge-lattice (*8*–*10*) or charge-spin (*11*) couplings. Oscillations in pump-probe traces are indicative of a coherent response involving low-energy excitations, and there are many examples in the literature of these oscillations in strongly correlated electronic materials (*11*–*13*). However, in a typical pump-probe experiment, it is difficult to distinguish between competing signal pathways and identify the origin of the coherent response. In most cases, the oscillations in the pump-probe data arise from displacive excitation of coherent phonons (*14*), usually optical phonons. Coherent acoustic phonons, excited by a stress gradient at the sample surface due to the laser absorption, have also been shown to generate oscillations as a result of the probe beam reflecting off the front of the shock wave and interfering with the reflection off the sample surface (*15*). In addition to phonons, low-energy coherent oscillations can also arise from the inherent order in the system and, thus, provide insight into the dominant interactions. The incoherent dynamics of these low-energy excitations can be obtained by measurements with infrared (IR)/terahertz (THz) pulses (*16*–*18*). For example, Matsunaga *et al.* (*16*) observed the Higgs amplitude mode in a Bardeen-Cooper-Schrieffer (BCS) superconductor using THz time-domain spectroscopy. On the other hand, Mansart *et al.* (*13*) attributed coherent oscillations in pump-probe measurements on a cuprate to coherent oscillations of the Cooper pair condensate. In this case, to make that attribution, the relevant oscillations were extracted from a series of pump-probe measurements, and a number of assumptions were made about the excitation process being impulsive stimulated Raman scattering. While potentially opening the door to new physics, this highlights one of the limitations of pump-probe measurements for revealing coherent dynamics: Many different pathways contribute to the nonlinear signal, and while coherent Raman-like pathways are expected to be present, the signal tends to be dominated by population effects and it is difficult to disentangle the different contributions.

Pump-probe experiments are a subclass of transient four-wave mixing (FWM) techniques that have been used for decades to measure dynamics (*4*, *17*, *19*). An FWM experiment on a simple two-level system is generally considered as follows: The first pulse generates a coherent superposition between ground and excited states, and the interaction with the second pulse converts this into a population. The third pulse converts this population into a coherent quantum superposition, which relaxes back to the ground state, emitting the signal. In pump-probe measurements, the first two interactions come from a single pulse—the pump, and the third pulse is the probe. The signal is then emitted in the same direction as the probe, and the interference between them gives the change in probe intensity.

For more complex samples that cannot be described as a two-level system, other pathways become possible. For example, instead of the first two pulses combining to excite a population, they can excite a coherent superposition of closely spaced energy states, in much the

[1]Centre for Quantum and Optical Science, Swinburne University of Technology, Hawthorn, Victoria 3122, Australia. [2]Department of Physical Chemistry II, Ruhr University Bochum, 44801 Bochum, Germany. [3]Department of Physics, University of Oxford, Oxford OX1 3PU, UK. [4]ARC Centre of Excellence for Future Low-Energy Electronics Technologies, Swinburne University of Technology, Hawthorn, Victoria 3122, Australia.
*Corresponding author. Email: jdavis@swin.edu.au

same manner as a coherent Raman experiment. Single-color transient grating experiments are another subclass of FWM, which has been applied to reveal the quasiparticle diffusion coefficients and scattering rates in $YBa_2Cu_3O_7$ (*20*). Like pump-probe experiments, these measurements probe population dynamics.

Other FWM approaches, however, can directly probe the coherent dynamics of quantum superpositions (*21*). To our knowledge, the measurement of these dynamics in a strongly correlated many-body electronic system has not been previously investigated. Multidimensional coherent spectroscopy (MDCS) (*22*) is an approach to FWM capable of precisely measuring coherent dynamics. It has been widely applied to semiconductors (*23*), molecules (*24*), and proteins (*25*, *26*), where it has enabled detailed understanding of relevant interactions. The key enhancement in MDCS over standard FWM experiments is that the phase of the signal is measured in addition to the amplitude. This is achieved by ensuring that the three excitation pulses are phase locked with each other and with a fourth pulse, the local oscillator (LO), which is overlapped with the signal for heterodyne detection. By recording the phase of the signal, both the real and imaginary parts of the response are simultaneously measured without the need of a Kramers-Kronig transformation.

Through the direct measurement of the phase information in MDCS, it becomes simpler to disentangle different pathways, allowing a greater level of control and insight into the interactions in strongly correlated electronic materials. Pathway-selective MDCS provides additional capability to separate different contributions: By controlling the spectral phase and amplitude of the excitation pulses, one can trigger and probe specific components, or pathways, of the nonlinear response of a material, such as pure quantum-coherent signals (*27*). Here, we use this approach to selectively excite and probe the dynamics of coherent quantum superpositions of low-energy excitations in a typical cuprate superconductor [$La_{2-x}Sr_xCuO_4$ (LSCO), $x = 15\%$, $T_C \sim 38$ K] in the strange metal phase ($T_{effective} \sim 50$ K). We found coherent dynamics persisting for ~500 fs originating directly from the quantum superposition of optically driven states with energy separation of 20 to 60 meV. Interactions with the third optical pulse reveal the correlation between these low-energy excitations and optically driven states at ~1.5 eV.

RESULTS AND DISCUSSION

Experimental description

The experiment is described schematically in Fig. 1: The first pulse, with wave vector $\mathbf{k_1}$ is spectrally shaped to be centered at 1.575 eV with full width at half maximum (FWHM) of 23 meV and a pulse duration of 80 fs; the second and third pulses, with wave vectors $\mathbf{k_2}$ and $\mathbf{k_3}$, respectively, are centered at 1.54 eV with an FWHM of 23 meV and a pulse duration of 77 fs, such that there is minimal spectral overlap with the first pulse. The first two pulses, which are set to arrive simultaneously, excite a coherent superposition between states, as indicated by the black oscillating curve in Fig. 1 (D and E). The spectral width of the pulses means that only quantum superpositions between states with energy separations ranging from about 20 to 60 meV will contribute to the measured signal beyond pulse

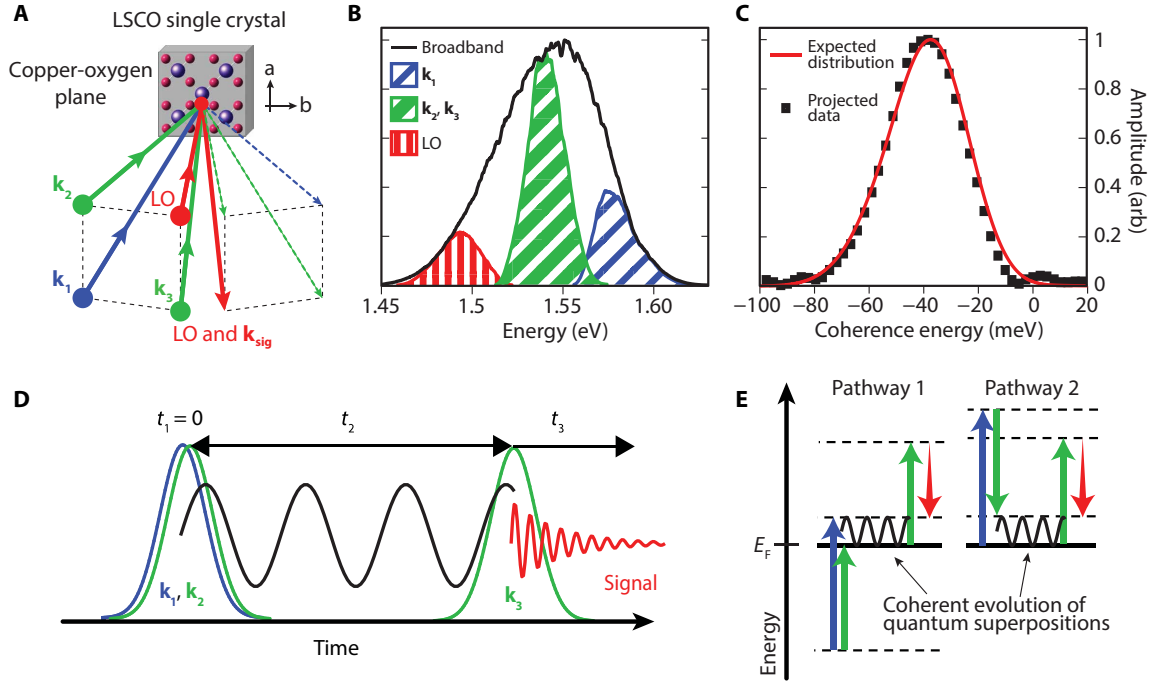

Fig. 1. Experimental scheme. (**A**) The geometry of the excitation is such that the three excitation pulses with wave vectors $\mathbf{k_1}$, $\mathbf{k_2}$, and $\mathbf{k_3}$ form three corners of a box with the LO on the fourth corner. The excitation is close to normal to the copper-oxygen plane, and the signal, which is overlapped with the LO, is measured in the reflected direction. (**B**) The shaped spectrum for each of the excitation pulses and the LO are shown together with the unshaped laser spectrum (black). (**C**) The convolution of $\mathbf{k_1}$ and $\mathbf{k_2}$ should determine the range of coherences that can be excited, shown in red. The data from the impulsive response from the sample (black squares) confirm this. (**D**) The first two nondegenerate pulses are overlapped in time, generating quantum superpositions between states separated by energies dependent on the pulse spectra shown in (C). The third pulse arrives at a controllable time, t_2, later and probes the coherent evolution of these superpositions through the emission of the signal (red). (**E**) Two possible signal pathways are depicted for the case of discrete energy levels. The coherent superpositions that are probed can be excited by two "upward" transitions (pathway 1) or an "up" and "down" transition (pathway 2) similar to a coherent Raman-like process.

overlap (Fig. 1C). This reduces the overall strength of the signal by eliminating the population pathways, which also reduces the noise level (*27*) and, thus, enhances the signal-to-noise ratio of the coherent response being probed. There are many possible pathways by which these coherences could be excited based on where the optical pulses are being absorbed/emitted to/from (see section S1 and fig. S1). Two such signal pathways are shown in Fig. 1E.

For the purposes of our discussion here, we focus on the state of the system after the first two pulses, at which point the sample is in a coherent quantum superposition of states separated by 20 to 60 meV. The third pulse, with an energy of 1.54 eV and wave vector $\mathbf{k_3}$, then interacts with this coherent superposition, leading to the third-order signal emitted in the phase-matched direction $\mathbf{k_s} = -\mathbf{k_1} + \mathbf{k_2} + \mathbf{k_3}$, with a central energy expected at ~1.505 eV. The emitted signal is overlapped with the LO and sent to a spectrometer where a spectral interferogram is measured and analyzed to provide the amplitude and phase of the signal. To probe the evolution of the coherent superposition excited by the first two pulses, we scanned the delay between the second and third pulses, t_2, and measured the evolution of the signal amplitude and phase. The sample was at a nominal temperature of 12 K, but the high repetition rate of 93 MHz and slow thermal relaxation cause the effective temperature to be higher. As detailed in section S2, we estimate the effective temperature of the sample during the experiments to be $T_{\text{effective}} \sim 50$ K ($T_{\text{effective}} \sim 80$ K) for the nominal temperature $T_{\text{nom}} = 12$ K ($T_{\text{nom}} = 66$ K). This pushes the sample above T_c (~38 K), indicating that we are not sensitive to the formation of the superconducting phase.

Measurements results

The real part of the measured signal is shown in Fig. 2A as a function of emission energy and delay time t_2; the integrated amplitude of the signal as a function of t_2 is shown in Fig. 2B. These show a strong response during pulse overlap and then a signal persisting out to $t_2 \sim 500$ fs, indicating that the quantum superpositions excited by the first two pulses remain coherent over this time scale. At pulse overlap, the peak signal corresponds to ~1500 signal photons/s, compared with a photon flux of ~4.5×10^{14}/s for each excitation beam. This signal strength is ~10^5 times smaller than the signal obtained from broadband measurements on GaAs quantum wells (*27*). To determine a value for the third-order susceptibility, we need to consider electric field amplitudes and get a value of $\chi^{(3)} \approx 2 \times 10^{-6}$.

The heterodyne detection not only helps to measure such a weak signal but also gives both the amplitude and phase of the signal electric field. As a result, the two-dimensional (2D) plot in Fig. 2A shows oscillations as a function of t_2, corresponding to the phase of the coherent superpositions that are excited in LSCO. The frequency of these oscillations appears to change as a function of the emission energy. To gain more insight into this signal, the data were Fourier transformed with respect to t_2 to generate the 2D spectrum in Fig. 2D. This 2D spectrum shows a narrow peak elongated along the

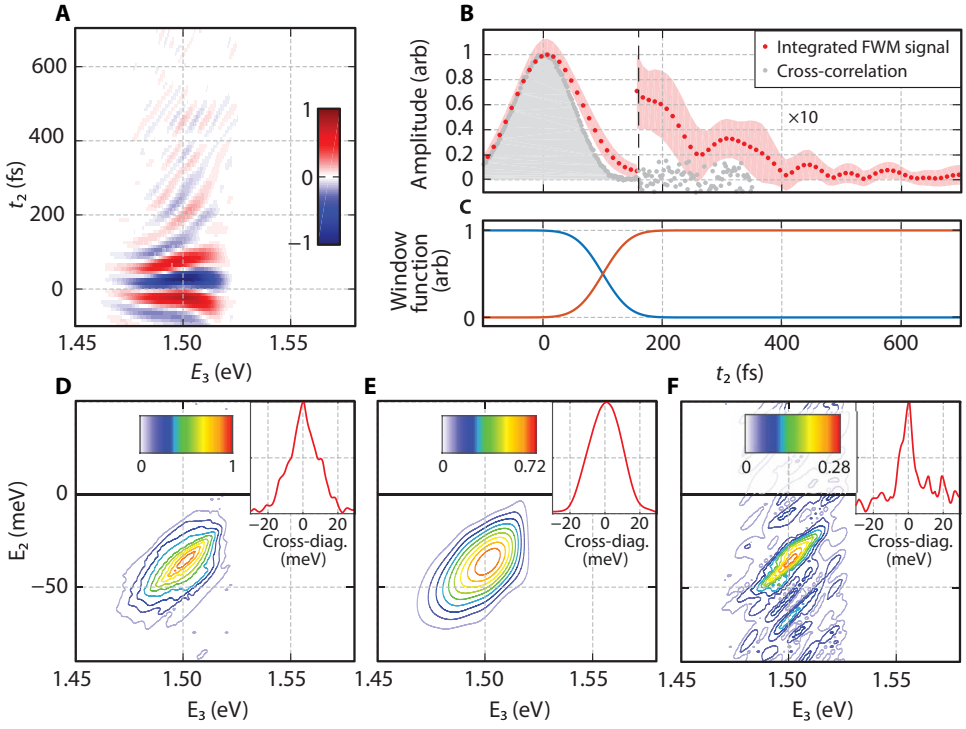

Fig. 2. Coherent dynamics of the low-energy excitations in LSCO. The temperature of the sample is $T_{\text{effective}} \sim 50$ K (see section S2), and LSCO is in the strange metal phase. (**A**) Real part of the spectrally resolved signal as a function of t_2: the delay between second and third pulses. The oscillating amplitude originates from the phase evolution of the coherent superposition excited by the first two pulses. The peak signal at pulse overlap corresponds to 1500 photons/s [$\chi^{(3)} \sim 2 \times 10^{-6}$]. (**B**) The spectrally integrated amplitude plotted as a function of t_2 shows the decay of the signal extending beyond 500 fs. The pulses cross-correlation is shown in gray. (**C**) Window functions used to isolate the response during pulse overlap (as wide as the cross-correlation of the pulses) and the response beyond pulse overlap. (**D**) The Fourier transform of the data with respect to t_2 yields the 2D spectrum, where E_2 corresponds to the coherence energy, i.e., the energy difference between the states in the quantum superposition. By windowing the data using the window functions shown in (C), the response at pulse overlap (**E**) and after pulse overlap (**F**) can be isolated. In (F), the diagonal peak shape corresponding to the extended signal becomes clear. In the insets of (D) to (F), a cross-diagonal slice of the respective 2D spectrum is plotted.

1:1 diagonal on top of a broader signal due to the response at pulse overlap. The cross section along the antidiagonal, shown in the inset of Fig. 2D, reveals a triangular peak shape typical of a Lorentzian on top of a broader Gaussian profile. By windowing the data in the t_2 domain, we can separate the response during pulse overlap, which contributes the broad part of the 2D spectrum, from the response after pulse overlap, which contributes the narrow Lorentzian part, as shown in Fig. 2 (E and F, respectively).

The 2D spectrum corresponding to the signal persisting beyond pulse overlap (Fig. 2F, obtained by windowing the data with the red function displayed in Fig. 2C), indicates that a signal is generated for a large distribution of coherence energies (E_2) or, in other words, that a broad distribution of low-energy states are coherently excited and contribute to the extended signal. The projection of the data onto the E_2 axis matches closely the distribution of energy differences expected between the first two pulses, as shown in Fig. 1C. For such a large distribution of coherence energies, one would normally expect the macroscopic coherence of the ensemble, and hence the measured signal, to decay rapidly (<50 fs) due to the different frequency components evolving to be out of phase. The expected 2D spectrum would then appear as a broad peak, matching the contribution that arises during pulse overlap (Fig. 2E). However, the results show that right across the distribution of coherence energies, there is a component that remains coherent for over ~500 fs, generating the narrow peak elongated along the diagonal in Fig. 2 (D and F), with a cross-diagonal width of ~9 meV.

The narrow diagonal peak is reminiscent of what is obtained in photon echo measurements, where rephasing of different frequencies allows homogeneous linewidths to be measured even in the presence of inhomogeneous broadening (*21*). In the present case, however, there is no rephasing, and the ability to observe the coherent evolution of quantum superpositions with a broad distribution of coherence energies is possible only because there is a correlation between the coherence energy (E_2) and the emission energy (E_3). This correlation is also evident in Fig. 2A, where the frequency of the oscillations varies as a function of the emission energy. This is directly mapped onto the 2D spectrum and leads to the narrow diagonal peak in Fig. 2F. The cross-diagonal width of this peak is then determined by the strength of the correlation and/or by the decoherence of the quantum superpositions.

Comparisons with vibrational coherence and a broad nonresonant response

To demonstrate that this response is not a typical response, we compare the data to two other samples, one with long-lived discrete vibrational coherences and one with no long-lived coherence. 2D spectra obtained for samples with clear discrete vibrational modes, as is the case for coherent optical phonons, show narrow peaks in E_2, which are spread across a range of E_3 values, as shown in Fig. 3B, for a laser dye molecule. This is typical of the 2D spectra normally expected for this type of experiment and is in stark contrast to what we observed for LSCO. On the basis of the time evolution of the signal amplitude for LSCO (Fig. 2B) and in the absence of the phase information, one would expect a narrow peak along the E_2 axis, similar to those observed for the laser dye (Fig. 3B). With the measurement of the phase information, however, it becomes possible to see the unexpected diagonal line shape for LSCO (Fig. 2F), which reveals the correlation of emission energy and coherence energy over the broad distribution of coherence energies excited.

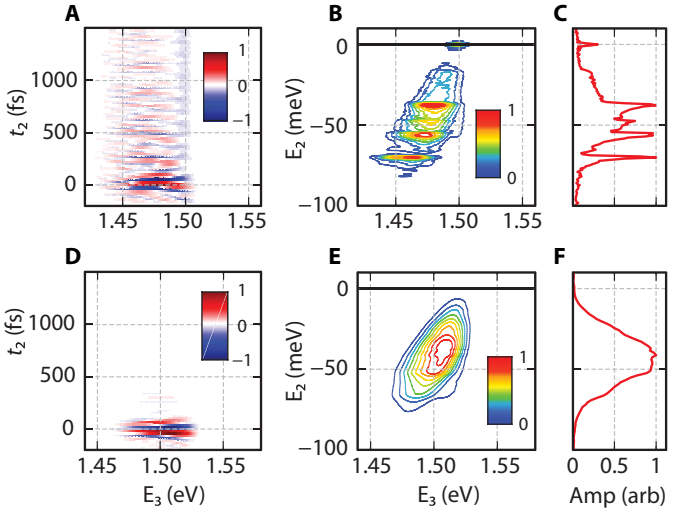

Fig. 3. Comparison with vibrational coherences and a broad nonresonant response. (**A**) Real part of the signal from IR813 laser dye, as a function of t_2 and E_3. The peak signal at pulse overlap corresponds to 3.3×10^6 photons/s [$\chi^{(3)} \sim 2 \times 10^{-4}$]. The response extends beyond 1500 fs with several oscillation frequencies. The normalized 2D spectrum (**B**) and projection on to the E_2 axis (**C**) show discrete narrow peaks corresponding to the discrete vibrational modes. Here, each peak is broad along the E_3 axis, matching the width of the third pulse. The signal amplitude beyond pulse overlap is about 10× larger for the molecular system (B) than for LSCO (Fig. 2F). (**D**) The real part of the signal from an $LiNbO_3$ crystal as a function of t_2 and E_3 shows the nonresonant response, which decays within the pulse overlap range. The peak signal at pulse overlap corresponds to 1×10^5 photons per second [$\chi^{(3)} \sim 2 \times 10^{-5}$]. The normalized 2D spectrum (**E**) and projection on to the E_2 axis (**F**) show broad peaks corresponding to the instrument response function. Further examination of the region beyond pulse overlap is shown in the Supplementary Materials. There is no evidence of any narrow diagonal peak in the nonresonant response.

Without this correlation, a broad distribution of coherences is expected to decay rapidly and within the pulse overlap regime. To confirm this, we repeated these measurements on a lithium niobate crystal. Lithium niobate has a relatively large and spectrally flat third-order nonlinearity, which means that a nonresonant response can be generated under the present excitation conditions. Figure 3D shows the response in the time domain, where the signal decays within the pulse overlap regime. The 2D spectrum (Fig. 3E) shows a broad diagonal peak, as expected for the pulse overlap response and similar to that seen in Fig. 2E for the response in the pulse overlap region for LSCO. The projection of this 2D spectrum onto the E_2 axis (Fig. 3F) reveals the broad distribution of coherences excited (covering the range of 20 to 60 meV). In these measurements, there is no hint of a narrow diagonal peak arising from an extended signal. A closer inspection of the signal beyond the pulse overlap does reveal some extended signal, albeit >10 times smaller than the response at the pulse overlap (compared with ~3 times smaller for the extended response in LSCO). Fourier transforming the data over this range of delays shows that this response is due to discrete vibration modes in $LiNbO_3$ (see section S5 for details). There is no indication of any narrow diagonal peak in the 2D spectrum, further confirming that the response we see in LSCO is due to the particular response of LSCO and not due to pulse overlap or any nonresonant response.

Model

Traditional analysis of MDCS data uses a perturbative approach to solve the Liouville variant of the Schrodinger equation in a single-particle

framework, with discrete states (*28*). For strongly correlated materials, such as optimally doped LSCO, the many-body nature of the different excitations and states should be taken into account for a full description and understanding of the experimental results. However, as we show below, a single-particle picture can still qualitatively reproduce the results and provide some physical insight into the correlations of this material. Here, we consider a modified three-level system, where each level is broadened, but the broadening between the top and bottom levels is correlated, as shown in Fig. 4A. After the first two pulses, the coherent superpositions between bands 1 and 2 (indicated by colored dashed arrows) are initiated with a distribution of coherence energies. The third pulse drives the system into a coherent superposition between bands 2 and 3 (black arrow), which radiates to give the signal (colored solid arrows pointing downward), leaving the system in band 2. This pathway is depicted in the Feynman-Liouville diagram in Fig. 4B. This modified three-level system shows how the correlation between the energy of the states in bands 1 and 3 leads to a correlation between the coherence energy, E_2, and the emission energy, E_3: An increase in coherence energy leads to a decrease in emission energy, and vice versa.

Figure 4 (C to F) shows the result of simulations in this framework, where we have introduced phenomenological decay terms to account for decoherence and relaxation and spectral widths to account for the broadening of the low-energy quantum coherence and the correlation between bands 1 and 3. Full details of the simulations, which are based on standard approaches for MDCS experiments, are given in Materials and Methods. As mentioned earlier, there are at least two factors that can affect the cross-diagonal width of the peak: correlation strength and decoherence (homogeneous linewidth). Thus, there is no unique set of parameters for a given 2D spectrum. In the case of the data in Fig. 4 (C to F), we used a Lorentzian linewidth of 80 meV for the transition between bands 1 and 3, decoherence time of 500 fs for the coherences between bands 1 and 2, and a width for the effective correlation of 4 meV (see Materials and Methods for details). It can be seen that the key experimental features (i.e., the extended signal in t_2 and the narrow diagonal peak in the 2D spectrum) are all reproduced in this simplified model. A corollary of the correlations observed is that in the 2D time-domain plot, the signal is shifted to negative times. This is observed in both experiment and simulation and can be described in the framework of "fast-light" (*29*) or pulse shaping, where a spectral phase gradient is generated by the distribution and evolution of coherence energies as described in section S3.

Signal origin

In conventional superconductivity, electronic excitations are "glued" into Cooper pairs by lattice vibrations (*30*). It has been suggested that a different kind of glue, for example, involving excitations at low energy, could be responsible for cuprate superconductivity (*31*). However, understanding the nature of these excitations and the absorption spectrum of the cuprates is puzzling (*32*). For the nonsuperconducting undoped systems, which appear as shiny metals to the naked eye, the optical absorption is dominated by charge-transfer gap transitions

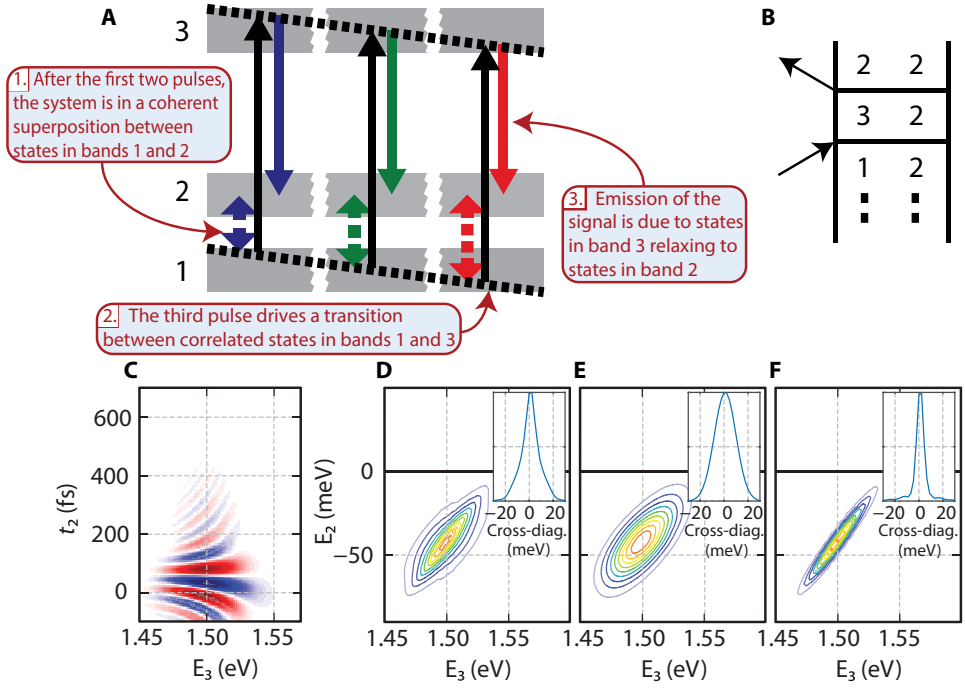

Fig. 4. Model and simulations for coherent response in LSCO. (**A**) The simple single-particle model shows the first two pulses generating quantum superpositions between bands 1 and 2 (dashed colored arrows), with a distribution of coherence energies. The third pulse (solid black vertical arrows) drives the transition to band 3 with energies correlated to those in band 1 (black dotted lines), leading to emission (solid colored arrows), which is anticorrelated with the coherence energy. (**B**) The corresponding Feynman diagram beginning with the coherent superposition between states in bands 1 and 2 triggered by the first two light-matter interactions. In (**C**) to (**F**), we show the results of simulations based on this picture. (C) The evolution of the real part of the signal, (D) the 2D spectrum of the full response, (E) the 2D spectrum from the response during pulse, and (F) the 2D spectrum from contribution making up the extended signal without pulse overlap. The insets show the corresponding cross-diagonal slices.

around 2 eV with a broad, asymmetrical, and long absorption tail, which extends to lower frequencies. When the system is chemically doped, the absorption below ~2 eV increases at the expense of spectral weight above the gap (*33*): The material develops a Drude peak with a frequency-dependent scattering rate (*32*) and a broad continuum of excitations extending to low frequency (including the 20 to 60 meV range measured here) with different symmetries (*34*). Both model calculations (*35*) and the similarly broad features observed in Raman spectroscopy (*36*) suggest that this broad continuum involves, in addition to magnetic (*37*) and vibrational (*32*, *33*) transitions, many-body excitations of different mixed atomic orbitals.

The nature of the low-energy coherent excitations observed here could be any one of these or indeed a combination of one or more (e.g., vibronic states of the correlated many-body system). At this stage, we cannot definitively identify the states with which our laser pulses are interacting; however, we consider some of the possible processes below.

The equilibrium band structure of optimally doped LSCO reveals a continuous density of states from well below the Fermi energy (E_F) level to well above it (*38*). It is then possible that states from about 1.55 eV (the laser photon energy) below E_F to ~1.55 eV above E_F can be involved in generating the nonlinear signal detected in our multidimensional experiment (see section S1 for possible pathways). Previous pump-probe experiments indicate that high-energy optical excitations decay on the tenths of a femtosecond time scale (*4*, *8*), while longer lifetimes have been found by angle-resolved photoemission spectroscopy measurements for excitations around E_F (*39*). This suggests that the quantum-coherent superpositions that persist for ~500 fs could involve states close to E_F. The first two interactions could then be considered as a coherent Raman-like process where we ignore any resonant interactions involving the first two pulses with higher-energy excitations. This is justified by data taken as a function of the delay between the first two pulses, t_1, and the corresponding 2D spectrum correlating E_1 and E_2, which shows none of the correlations seen in Fig. 2 (see section S4).

Previous Raman measurements on similar samples revealed a smooth, essentially featureless spectrum over the range of E_2 energies probed here (*34*, *36*). Raman modes of different symmetry (primarily A_{1g}, B_{1g}, and B_{2g}) have been identified by polarization controlled experiments, with the two modes with B symmetry (B_{1g} and B_{2g}) being of particular interest for their possible role in the pairing mechanism (*13*). We have repeated our MDCS measurements with different polarization combinations, as shown in Fig. 5. These results reveal little difference between colinear and cocircular excitation, but the peak intensity drops to 50% of the amplitude for cross-circular and ~10% for cross-linear excitation. With the caveat that we expect that the surface stress is minimal in our samples (*40*), these results are not consistent with the trends expected for a Raman process involving modes with A or B symmetry: for B_{1g} or B_{2g} symmetry, one would expect no difference between colinear and cross-linear excitation but complete cancelation of the signal in going from cocircular to cross-circular (*34*). For acoustic modes with A_{1g} symmetry, one would expect complete cancelation for both cross-linear and cross-circular polarization sequences (*34*). These results confirm that while the signal we observe is similar to a simple Raman measurement with nonresonant optical fields, this cannot completely describe the results and the interaction with a higher energy level (band 3 in Fig. 4) is required. Last, regardless of the possible surface stress (*40*), the signal is strongly suppressed for the cross-linear configuration, suggesting that the excitation triggered by the third pulse should be close to a linear dipole transition, like a charge-transfer excitation.

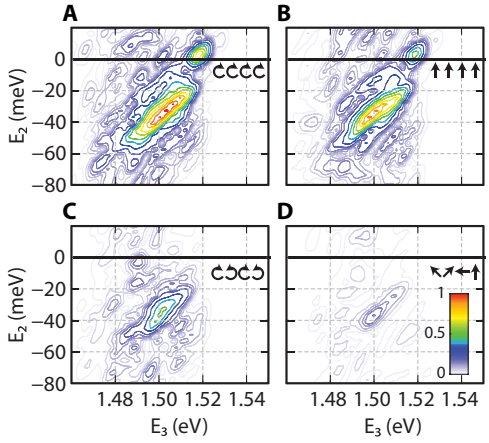

Fig. 5. Polarization-dependent 2D spectra in LSCO. The temperature of the sample is $T_{effective}$ ~ 50 K (see section S2), and LSCO is in the strange metal phase. The 2D spectra from the extended part of the signal for (**A**) cocircular, (**B**) colinear, (**C**) cross-circular, and (**D**) cross-linear excitation are shown. The narrow diagonal peak shape remains unchanged, and only the amplitude varies for the different polarization combinations.

Recent pump-probe measurements by Miyamoto *et al.* (*11*) on the Mott insulator Nd_2CuO_4 showed oscillations with frequency that depends on the probe energy. This trend is similar to what we observe here (Fig. 2F) and may have the same origin. Miyamoto *et al.* (*11*) explained these oscillations as polarization beating between different pathways involving two magnon excitations. However, there are some important aspects of the results that are not explained within their model, including the relatively long coherence time/narrow linewidth implied in their measurements and identified here. One of the advantages of MDCS is that it measures the phase of the signal and its evolution, which means the coherent response measured here can only come from quantum superpositions in the sample and not polarization beating. The correlation between the states at low and high energy that we identify here as a result of this phase evolution could also underlie some of the unexpected behavior in the pump-probe results on Nd_2CuO_4 *(11)*. The challenge remains, however, to understand the origin and nature of these correlations.

CONCLUSIONS

Here, we applied MDCS to a prototypical many-body quantum material, LSCO, and found novel quantum signatures: a ~500-fs-long coherent signal originating from the superpositions of many-body states at low energy. We found a strong correlation between the energy of this coherence and the optical energy of the emitted signal, which indicates a coherent interaction between the states at low and high energy in these complex systems.

A fundamental concept valid for correlated electronic materials, which is at odds with single-particle theories, is that when the number of available excitations change by, e.g., chemical substitution (*32*) or photodoping (*3*, *6*), so too does the band structure (*33*, *35*, *38*). Thus, the effective energy structure of the sample can change transiently as the measurement proceeds, which can lead to links between low-energy excitations and optically excited electronic states. We propose that it is these interactions that lead to the correlations that we measure between the coherent quantum superpositions with an

energy of 20 to 60 meV and an optically driven states of ~1.55 eV above this. Beyond the specific interpretations, these results demonstrate that MDCS is a powerful tool to study electronic correlations and opens the door to addressing directly the quantum-coherent states of many-body matter.

MATERIALS AND METHODS

Sample details

The crystal was grown by using the flux technique. Stoichiometric amounts of high-purity (>99.99%) La_2O_3, $SrCO_3$, and CuO chemicals were mixed. Furthermore, 75 mole percent of CuO was added as flux. These powders were placed in a platinum crucible, covered tightly with a platinum lid, and heated in a chamber furnace. The crucible was heated to 1250°C and kept there for 10 hours, and then it was slowly cooled down to 1100°C at a rate of 2°C/hour. After the growth, the flux was separated by inverting the crucible when it was at 1100°C. Last, the furnace was cooled down to room temperature at the rate of 50°C/hour. (*41*). The grown crystals were annealed under oxygen flow to increase the T_C and cooled very slowly down to room temperature, so that the strain should be reduced to a minimum. The Sr doping was 0.15, and it was checked by the electron probe microanalysis technique. The magnetic properties were measured using SQUID (superconducting quantum interference device) magnetometry.

Measurements details

The transient FWM experiments were performed using the experimental apparatus described previously (*27*, *42*). It uses a Ti:sapphire oscillator generating pulses centered at ~1.55 eV and spectrum shown in Fig. 1B (black) at a repetition rate of 93 MHz. The laser output was compressed using a folded prism compressor and split into the four beams in a box geometry by a beam shaper, consisting of a 2D grating pattern applied to a spatial light modulator (SLM). The four beams were collected by a lens and propagated through all common optics, in a 4F geometry, to ensure a high level of phase stability between all four beams. They were incident on an SLM-based pulse shaper, which allows independent control of the spectral amplitude and phase for each of the four beams. The spectral phase was first optimized to ensure properly compressed pulses by performing spectrally resolved cross-correlations of each pair of pulses. A spectral phase described by a fourth-order polynomial was applied in the SLM pulse shaper, with the coefficients varied to optimize the cross-correlations and minimize the pulse durations. Similar results were obtained by using a dispersion scan approach (*43*) to optimize the spectral phase on each pulse individually. The pulse duration of the unshaped pulse was 25 fs. The spectral amplitude of the three excitation pulses and LO were shaped to give the spectra shown in Fig. 1B (colored). Cross-correlations of the individual shaped pulses with an unshaped pulse were performed, and spectral phase optimizations were repeated to ensure a flat spectral phase. The pulse durations for these shaped pulses were 80 fs (pulse 1) and 77 fs (pulses 2 and 3).

To control the timing of each pulse, and hence the interpulse delays, independent spectral phase gradients were applied to each pulse. The LO was attenuated and delayed by a neutral density filter, and the four beams were focused onto the sample with a 20-cm lens.

The signal generated in the phase-matched direction $-(-\mathbf{k_1} + \mathbf{k_2} + \mathbf{k_3})$ was spatially overlapped with the LO, which copropagates into a spectrometer where a spectral interferogram is detected, providing details of the signal amplitude and phase. Other signals originating from different wave mixing are emitted in very different directions and were not detected. An eight-step phase cycling procedure was used to isolate the signal from background scatter and enhanced the signal-to-noise ratio.

In the measurements reported here, data were acquired by setting the delay between the first and second pulses to zero ($t_1 = 0$) and increasing the delay of the third pulse (t_2) by controlling its spectral phase. From this series of interferograms, the time-resolved signal can be obtained as shown in Fig. 2A. Fourier transforms of the data with respect to t_2 lead to the 2D spectra in Fig. 2 (D to F). The average power in each excitation beam for these experiments was 400 μW. Additional measurements at different intensities were performed to ensure that these experiments were being done in a third-order regime. The linear polarization–dependent experiments were performed by introducing a half-wave plate and linear polarizer into each beam and setting the polarizations accordingly. For the circularly polarized experiments (Fig. 5), an additional quarter-wave plate was introduced after the linear polarizers to convert the linear polarizations to circular polarization. The LSCO samples were mounted in a temperature-controlled recirculating cryostat. Measurements were recorded with the sample temperature nominally at 12 and 66 K and give consistent results, indicating the superconducting phase was thermally melted (see section S2).

The laser polarization was in the copper-oxygen a-b plane of LSCO, and the signal is independent of the sample orientation in the a-b plane (e.g., if the laser fields are parallel, perpendicular, or in between a and b).

Simulation

We simulated the nonlinear response of LSCO by numerically solving the Liouville variant of the Schrodinger equation for the three-level system described in Fig. 4 (A and B)

$$i\hbar\dot{\rho} = [H, \rho]$$

with $H = H_0 + H_{\text{int}} + H_{\text{relax}}$

$$H_0 = \begin{bmatrix} \epsilon_1 & 0 & 0 \\ 0 & \epsilon_2 & 0 \\ 0 & 0 & \epsilon_3 \end{bmatrix}, H_{\text{int}} = \begin{bmatrix} 0 & 0 & E(\mathbf{k},t)\,\mu_{13} \\ 0 & 0 & E(\mathbf{k},t)\,\mu_{23} \\ E^*(\mathbf{k},t)\,\mu_{13}^* & E^*(\mathbf{k},t)\,\mu_{23}^* & 0 \end{bmatrix};$$

$$[H_{\text{relax}}, \rho] = -i\hbar\,\gamma_{ij}\,\rho_{ij}$$

where ϵ_i is the energy of state i; μ_{ij} is the transition dipole moment for the transition between state i and j; and γ_{ij} is the phenomenological decay rate for each term in the density matrix, ρ_{ij}, which corresponds to a population lifetime where $i = j$, and decoherence time where $i \neq j$. The rotating wave approximation was made, and the electric field of the excitation pulses, $E(\mathbf{k}, t)$, is given by

$$E(\mathbf{k},t) = E_1(t)\,e^{i(\mathbf{k}_1\cdot\boldsymbol{r}-\omega_1 t)} + E_2(t)\,e^{i(\mathbf{k}_2\cdot\boldsymbol{r}-\omega_2 t)} + E_3(t)\,e^{i(\mathbf{k}_3\cdot\boldsymbol{r}-\omega_3 t)}$$

where $\mathbf{k}_i$ is the wave vector, ω_i the frequency, and $E_i(t)$ is the real valued Gaussian envelope function of pulse i, with width given by the experimental pulse durations. The electric field was treated perturbatively, and the system of equations was expanded up to third order, with the emitted signal being proportional to the third-order polarization, corresponding to $\mu_{13}\rho_{13}^{(3)}$, with wavevector $-\mathbf{k_1} + \mathbf{k_2} + \mathbf{k_3}$. The resultant set of interdependent differential equations was numerically solved to facilitate the use of realistic pulses with finite duration.

We took the dipole moment for the transition between states 1 and 3 (μ_{13}) to be the same as the one between states 2 and 3 (μ_{23}). The homogeneous linewidths of these transitions (γ_{13} and γ_{23}) were set to 80 meV, such that the ~1.55-eV coherent superpositions decay within the pulse duration, as observed in the projection of the 3D spectrum onto the one-quantum 2D spectrum shown in fig. S4. The homogeneous linewidth γ_{12} of the zero-quantum coherence transition was set to 8 meV, corresponding to a decay time of 500 fs. The energies of states 1 and 3 were kept fixed at 0 and 1.54 eV, and to account for the distribution of coherence energies, the simulation was run for different values of ϵ_2 and the results were summed, weighted by a Gaussian distribution centered at 40 meV with 40-meV FWHM. By varying the energy of state 2, the energy differences between 1 and 2 and between 2 and 3 were anticorrelated, as described in Fig. 4A, and observed in the experiments. The strength of the correlation between bands 1 and 3 was controlled by adjusting the effective spectral width of the third pulse, which drives the transition indicated by the black line in Fig. 4A. For the data shown in Fig. 4E, corresponding to the case where the long-lived coherences were observed, this width was set to 4 meV. For Fig. 4D, where the pulse overlap regime is simulated, this width was set to 30 meV, and in Fig. 4C, the sum of these two contributions was plotted.

SUPPLEMENTARY MATERIALS

Supplementary material for this article is available at http://advances.sciencemag.org/cgi/content/full/6/9/eaaw9932/DC1

Section S1. Possible pathways for excitation of the 40 ± 20–meV coherent superpositions
Section S2. Heating effects due to laser excitation
Section S3. Emission at negative times
Section S4. Correlations between E_1, E_2, and E_3
Section S5. Response from $LiNbO_3$
Fig. S1. Signal pathways.
Fig. S2. Thermal effects.
Fig. S3. Apparent signal at negative delays.
Fig. S4. 3D spectra from LSCO and projection onto the 2D planes.
Fig. S5. Windowed 2D spectra from $LiNbO_3$.
References (*44*–*51*)

REFERENCES AND NOTES

1. Y. Tokura, M. Kawasaki, N. Nagaosa, Emergent functions of quantum materials. *Nat. Phys.* **13**, 1056–1068 (2017).
2. E. Dagotto, Complexity in strongly correlated electronic systems. *Science* **309**, 257–262 (2005).
3. J. Zhang, R. D. Averitt, Dynamics and control in complex transition metal oxides. *Annu. Rev. Mat. Res.* **44**, 19–43 (2014).
4. C. Giannetti, M. Capone, D. Fausti, M. Fabrizio, F. Parmigiani, D. Mihailovic, Ultrafast optical spectroscopy of strongly correlated materials and high-temperature superconductors: A non-equilibrium approach. *Adv. Phys.* **65**, 58–238 (2016).
5. H. Kishida, M. Ono, A. Sawa, M. Kawasaki, Y. Tokura, H. Okamoto, Third-order nonlinear optical spectroscopy in the two-dimensional cuprates Nd_2CuO_4 and La_2CuO_4. *Phys. Rev. B* **68**, 075101 (2003).
6. H. Okamoto, T. Miyagoe, K. Kobayashi, H. Uemura, H. Nishioka, H. Matsuzaki, A. Sawa, Y. Tokura, Photoinduced transition from Mott insulator to metal in the undoped cuprates Nd_2CuO_4 and La_2CuO_4. *Phys. Rev. B* **83**, 125102 (2011).
7. C. Gadermaier, V. V. Kabanov, A. S. Alexandrov, L. Stojchevska, T. Mertelj, C. Manzoni, G. Cerullo, N. D. Zhigadlo, J. Karpinski, Y. Q. Cai, X. Yao, Y. Toda, M. Oda, S. Sugai, D. Mihailovic, Strain-induced enhancement of the electron energy relaxation in strongly correlated superconductors. *Phys. Rev. X* **4**, 011056 (2014).
8. S. Dal Conte, L. Vidmar, D. Golež, M. Mierzejewski, G. Soavi, S. Peli, F. Banfi, G. Ferrini, R. Comin, B. M. Ludbrook, L. Chauviere, N. D. Zhigadlo, H. Eisaki, M. Greven, S. Lupi, A. Damascelli, D. Brida, M. Capone, J. Bonča, G. Cerullo, C. Giannetti, Snapshots of the retarded interaction of charge carriers with ultrafast fluctuations in cuprates. *Nat. Phys.* **11**, 421–426 (2015).
9. L. Perfetti, P. A. Loukakos, M. Lisowski, U. Bovensiepen, H. Eisaki, M. Wolf, Ultrafast electron relaxation in superconducting $Bi_2Sr_2CaCu_2O_{8+\delta}$ by time-resolved photoelectron spectroscopy. *Phys. Rev. Lett.* **99**, 197001 (2007).
10. J. Kogoj, M. Mierzejewski, J. Bonča, Nature of bosonic excitations revealed by high-energy charge carriers. *Phys. Rev. Lett.* **117**, 227002 (2016).
11. T. Miyamoto, Y. Matsui, T. Terashige, T. Morimoto, N. Sono, H. Yada, S. Ishihara, Y. Watanabe, S. Adachi, T. Ito, K. Oka, A. Sawa, H. Okamoto, Probing ultrafast spin-relaxation and precession dynamics in a cuprate Mott insulator with seven-femtosecond optical pulses. *Nat. Commun.* **9**, 3948 (2018).
12. W. Albrecht, T. Kruse, H. Kurz, Time-resolved observation of coherent phonons in superconducting $YBa_2Cu_3O_{7-\delta}$ thin films. *Phys. Rev. Lett.* **69**, 1451–1454 (1992).
13. B. Mansart, J. Lorenzana, A. Mann, A. Odeh, M. Scarongella, M. Chergui, F. Carbone, Coupling of a high-energy excitation to superconducting quasiparticles in a cuprate from coherent charge fluctuation spectroscopy. *Proc. Natl. Acad. Sci. U.S.A.* **110**, 4539–4544 (2013).
14. T. E. Stevens, J. Kuhl, R. Merlin, Coherent phonon generation and the two stimulated Raman tensors. *Phys. Rev. B* **65**, 144304 (2002).
15. D. Lim, V. Thorsmølle, R. Averitt, Q. X. Jia, K. H. Ahn, M. J. Graf, S. A. Trugman, A. J. Taylor, Coherent optical and acoustic phonon generation correlated with the charge-ordering phase transition in $La_{1-x}Ca_xMnO_3$. *Phys. Rev. B* **71**, 134403 (2005).
16. R. Matsunaga, Y. I. Hamada, K. Makise, Y. Uzawa, H. Terai, Z. Wang, R. Shimano, Higgs amplitude mode in the BCS superconductors $Nb_{1-x}Ti_xN$ induced by terahertz pulse excitation. *Phys. Rev. Lett.* **111**, 057002 (2013).
17. A. Pashkin, M. Porer, M. Beyer, K. W. Kim, A. Dubroka, C. Bernhard, X. Yao, Y. Dagan, R. Hackl, A. Erb, J. Demsar, R. Huber, A. Leitenstorfer, Femtosecond response of quasiparticles and phonons in superconducting $YBa_2Cu_3O_{7-\delta}$ studied by wideband terahertz spectroscopy. *Phys. Rev. Lett.* **105**, 067001 (2010).
18. F. Novelli, G. De Filippis, V. Cataudella, M. Esposito, I. Vergara, F. Cilento, E. Sindici, A. Amaricci, C. Giannetti, D. Prabhakaran, S. Wall, A. Perucchi, S. Dal Conte, G. Cerullo, M. Capone, A. Mishchenko, M. Grüninger, N. Nagaosa, F. Parmigiani, D. Fausti, Witnessing the formation and relaxation of dressed quasi-particles in a strongly correlated electron system. *Nat. Commun.* **5**, 5112 (2014).
19. S. Mukamel, *Principles of Nonlinear Optical Spectroscopy* (Oxford Univ. Press, 1995).
20. N. Gedik, J. Orenstein, R. Liang, D. A. Bonn, W. N. Hardy, Diffusion of nonequilibrium quasi-particles in a cuprate superconductor. *Science* **300**, 1410–1412 (2003).
21. P. Borri, W. Langbein, S. Schneider, U. Woggon, R. Sellin, D. Ouyang, D. Bimberg, Ultralong dephasing time in InGaAs quantum dots. *Phys. Rev. Lett.* **87**, 157401 (2001).
22. D. M. Jonas, Two-dimensional femtosecond spectroscopy. *Annu. Rev. Phys. Chem.* **54**, 425–463 (2003).
23. G. Moody, S. T. Cundiff, Advances in multi-dimensional coherent spectroscopy of semiconductor nanostructures. *Adv. Phys. X* **2**, 641–674 (2017).
24. I. Breen, R. Tempelaar, L. A. Bizimana, B. Kloss, D. R. Reichman, D. B. Turner, Triplet separation drives singlet fission after femtosecond correlated triplet pair production in rubrene. *J. Am. Chem. Soc.* **139**, 11745–11751 (2017).
25. J. T. King, E. J. Arthur, C. L. Brooks III, K. J. Kubarych, Crowding induced collective hydration of biological macromolecules over extended distances. *J. Am. Chem. Soc.* **136**, 188–194 (2014).
26. E. Collini, C. Y. Wong, K. E. Wilk, P. M. G. Curmi, P. Brumer, G. D. Scholes, Coherently wired light-harvesting in photosynthetic marine algae at ambient temperature. *Nature* **463**, 644–647 (2010).
27. J. O. Tollerud, C. R. Hall, J. A. Davis, Isolating quantum coherence using coherent multi-dimensional spectroscopy with spectrally shaped pulses. *Opt. Express* **22**, 6719–6733 (2014).
28. G. Nardin, G. Moody, R. Singh, T. M. Autry, H. Li, F. Morier-Genoud, S. T. Cundiff, Coherent excitonic coupling in an asymmetric double InGaAs quantum well arises from many-body effects. *Phys. Rev. Lett.* **112**, 046402 (2014).
29. M. S. Bigelow, N. N. Lepeshkin, R. W. Boyd, Superluminal and slow light propagation in a room-temperature solid. *Science* **301**, 200–202 (2003).
30. A. P. Drozdov, M. I. Eremets, I. A. Troyan, V. Ksenofontov, S. I. Shylin, Conventional superconductivity at 203 kelvin at high pressures in the sulfur hydride system. *Nature* **525**, 73–76 (2015).
31. D. J. Scalapino, A common thread: The pairing interaction for unconventional superconductors. *Rev. Mod. Phys.* **84**, 1383–1417 (2012).
32. D. Basov, T. Timusk, Electrodynamics of high-*Tc* superconductors. *Rev. Mod. Phys.* **77**, 721–779 (2005).
33. S. Uchida, T. Ido, H. Takagi, T. Arima, Y. Tokura, S. Tajima, Optical spectra of $La_{2-x}Sr_xCuO_4$: Effect of carrier doping on the electronic structure of the CuO_2 plane. *Phys. Rev. B* **43**, 7942–7954 (1991).
34. T. P. Devereaux, R. Hackl, Inelastic light scattering from correlated electrons. *Rev. Mod. Phys.* **79**, 175–233 (2007).
35. C. Weber, K. Haule, G. Kotliar, Optical weights and waterfalls in doped charge-transfer insulators: A local density approximation and dynamical mean-field theory study of $La_{2-x}Sr_xCuO_4$. *Phys. Rev. B* **78**, 134519 (2008).
36. S. Caprara, C. di Castro, B. Muschler, W. Prestel, R. Hackl, M. Lambacher, A. Erb, S. Komiya, Y. Ando, M. Grilli, Extracting the dynamical effective interaction and competing order

from an analysis of Raman spectra of the high-temperature $La_{2-x}Sr_xCuO_4$ superconductor. *Phys. Rev. B* **84**, 054508 (2011).
37. J. Lorenzana, G. A. Sawatzky, Phonon assisted multimagnon optical absorption and long lived two-magnon states in undoped lamellar copper oxides. *Phys. Rev. Lett.* **74**, 1867–1870 (1995).
38. A. Damascelli, Z. Hussain, Z.-X. Shen, Angle-resolved photoemission studies of the cuprate superconductors. *Rev. Mod. Phys.* **75**, 473–541 (2003).
39. J. D. Rameau, S. Freutel, A. F. Kemper, M. A. Sentef, J. K. Freericks, I. Avigo, M. Ligges, L. Rettig, Y. Yoshida, H. Eisaki, J. Schneeloch, R. D. Zhong, Z. J. Xu, G. D. Gu, P. D. Johnson, U. Bovensiepen, Energy dissipation from a correlated system driven out of equilibrium. *Nat. Commun.* **7**, 13761 (2016).
40. H.-H. Kung, R. E. Baumbach, E. D. Bauer, V. K. Thorsmolle, W. L. Zhang, K. Haule, J. A. Mydosh, G. Blumberg, Chirality density wave of the "hidden order" phase in URu2Si2. *Science* **347**, 1339–1342 (2015).
41. C. Chen, B. E. Watts, B. M. Wanklyn, P. A. Thomas, P. W. Haycock, Phase diagram and single crystal growth of $(La, Sr)_2CuO_4$ from CuO solution. *J. Cryst. Growth* **91**, 659–665 (1988).
42. J. O. Tollerud, J. A. Davis, Coherent multi-dimensional spectroscopy: Experimental considerations, direct comparisons and new capabilities. *Prog. Quantum Electron.* **55**, 1–34 (2017).
43. M. Miranda, C. L. Arnold, T. Fordell, F. Silva, B. Alonso, R. Weigand, A. L'Huillier, H. Crespo, Characterization of broadband few-cycle laser pulses with the d-scan technique. *Opt. Express* **20**, 18732–18743 (2012).
44. C. Weber, K. Haule, G. Kotliar, Apical oxygens and correlation strength in electron- and hole-doped copper oxides. *Phys. Rev. B* **82**, 125107 (2010).
45. Z. Qin, J. C. Bischof, Thermophysical and biological responses of gold nanoparticle laser heating. *Chem. Soc. Rev.* **41**, 1191–1217 (2012).
46. X. F. Sun, J. Takeya, S. Komiya, Y. Ando, Thermal conductivity of lightly Sr- and Zn-doped La2CuO4 singla crystals. *Phys. Rev. B* **67**, 104503 (2003).
47. D. T. Morelli, J. Heremans, G. Doll, P. J. Picone, H. P. Jenssen, M. S. Dresselhaus, Thermal properties of single-crystal$La_2CuO_{4-\Delta}$. *Phys. Rev. B* **39**, 804–807 (1989).
48. S. Chu, S. Wong, Linear pulse-propagation in an absorbing medium. *Phys. Rev. Lett.* **48**, 738–741 (1982).
49. A. M. Akulshin, S. Barreiro, A. Lezama, Steep Anomalous Dispersion in Coherently Prepared Rb Vapor. *Phys. Rev. Lett.* **83**, 4277–4280 (1999).
50. L. J. Wang, A. Kuzmich, A. Dogariu, Gain-assisted superluminal light propagation. *Nature* **406**, 277–279 (2000).
51. R. F. Schaufele, M. J. Weber, Raman Scattering by Lithium Niobate. *Phys. Rev.* **152**, 705–708 (1966).

Acknowledgments: F.N. acknowledges F. Cilento, D. Fausti, A. Avella, and F. Parmigiani for discussions. **Funding:** This research was supported in part by the Australian Research Council Centre of Excellence in Future Low-Energy Electronics Technologies (FLEET), project no. CE170100039, and by an ARC Future Fellowship (FT120100587). **Author contributions:** F.N. proposed the experiment. J.O.T. performed the measurements with help from F.N. J.O.T. and J.A.D. developed the optical setup. J.O.T. and J.A.D. analyzed the data and prepared the figures with help from F.N. J.A.D. developed the model and performed the simulations. D.P. fabricated and provided high-quality samples. J.A.D. and F.N. wrote the manuscript with help from all authors. **Competing interests:** The authors declare that they have no competing interests. **Data and materials availability:** All data needed to evaluate the conclusions in the paper are present in the paper and/or the Supplementary Materials. Additional data related to this paper may be requested from the authors.

Submitted 13 February 2019
Accepted 5 December 2019
Published 28 February 2020
10.1126/sciadv.aaw9932

Citation: F. Novelli, J. O. Tollerud, D. Prabhakaran, J. A. Davis, Persistent coherence of quantum superpositions in an optimally doped cuprate revealed by 2D spectroscopy. *Sci. Adv.* **6**, eaaw9932 (2020).

Science Advances

Persistent coherence of quantum superpositions in an optimally doped cuprate revealed by 2D spectroscopy

Fabio Novelli, Jonathan O. Tollerud, Dharmalingam Prabhakaran and Jeffrey A. Davis

Sci Adv **6** (9), eaaw9932.
DOI: 10.1126/sciadv.aaw9932